GNSS NLOS Exclusion Based on Dynamic Object Detection Using LiDAR Point Cloud

Weisong Wen, Guohao Zhang, and Li-Ta Hsu

Abstract—**Absolute positioning is an essential factor for the arrival of autonomous driving. At present, GNSS is the indispensable source that can supply initial positioning in the commonly used high definition map-based LiDAR point cloud positioning solution for autonomous driving. However, the non-light-of-sight (NLOS) reception dominates GNSS positioning performance in super-urbanized areas. The recent proposed 3D map aided (3DMA) GNSS can mitigate the majority of the NLOS caused by buildings. However, the same phenomenon caused by moving objects in urban areas is currently not modeled in the 3D geographic information system (GIS). Therefore, we present a novel method to exclude the NLOS receptions caused by a double-decker bus, one of the symbolic tall moving objects in road transportations. To estimate the dimension and orientation of the double-decker buses relative to the GNSS receiver, LiDAR-based perception is utilized. By projecting the relative positions into GNSS Skyplot, the direct transmission path of satellite signals blocked by the moving objects can be identified and excluded from positioning. Finally, GNSS positioning is estimated by the weighted least square (WLS) method based on the remaining satellites after the NLOS exclusion. Both static and dynamic experiments are conducted in Hong Kong. The results show that the proposed NLOS exclusion using LiDAR-based perception can greatly improve the GNSS single point positioning (SPP) performance.**

Index Terms—**GPS, GNSS, NLOS, LiDAR, 3D point clouds, object detection, positioning.**

I. INTRODUCTION

To ACHIEVE fully autonomous driving in highly urbanized areas, absolute lane-level positioning is required. Light detection and ranging (LiDAR), cameras and inertial navigation systems (INS) are usually integrated with GNSS positioning [1]–[3]. However, the three positioning sources can only conduct relative positioning. The GNSS/INS/LiDAR/ high definition map-based [1] positioning is the potential solution to provide robust and constant localization information for autonomous driving. In this solution, the searching for the initial position in the existing high definition map is essential. GNSS is currently the key source providing

the initial absolute positioning information. GNSS solution possesses increased popularity because of the availability of multi-constellation global navigation satellite systems (GPS, BeiDou, GLONASS, Galileo, and QZSS). GNSS positioning can obtain decent performance if the GNSS receiver receives enough direct signals transmitted from satellites, so-called line-of-sight (LOS) [4]. However, the GNSS propagation may be reflected, diffracted or blocked by skyscrapers and moving objects in highly urbanized areas, such as Hong Kong, which can cause additional signal transmission delay. Thus, it introduces pseudorange errors as both multipath effects and non-light-of-sight (NLOS) receptions can cause a positioning error of more than 100 meters in deep urban canyons [5], [6].

According to a recent paper survey, NLOS is the main challenge for GNSS urban localization [7]. In nature, buildings reflect and block the GNSS signal causing NLOS. Thus, the use of a 3D building model to aid GNSS positioning is straightforward [8]. Based on the 3D building model, the NLOS measurement can be excluded from GNSS positioning if the prior knowledge of the user position is available [9]–[11]. However, excluding all the NLOS measurements will result in a distortion of satellite distribution. This large dilution of precision (DOP) will enlarge the GNSS positioning error in a lateral direction which is not welcomed for the application of intelligent transportation systems [12], [13]. One of the most famous methods is called GNSS shadow matching, which is to compare the measured satellite visibilities with that of a group of hypothesized positions [14]–[16]. This method greatly improves the positioning performance in the lateral direction by using the NMEA level of the GNSS message [17]. To further improve the positioning accuracy, a ray-tracing simulation is conducted to track the signal transmission paths (both direct and reflect) within the 3D building models [18]. By this ray-tracing simulation, the NLOS is not only detected but also corrected [19], [20]. GNSS shadow matching and the range-based 3D maps aided positioning method are combined to optimize the GNSS positioning result in urban canyons [21]. Recently, the researches to waive the 3D building model with different levels of prior information of the city is studied [22], [23].

The 3D laser scanner is also used to construct the point cloud-based 3D geographic information of buildings, so-called 3D point cloud map. The 3D point cloud map is employed to detect the visibilities of satellites [24]. To better model the reliability of GNSS positioning, horizontal dilution of precision (HDOP) is calculated using the remaining satellites and signal noise ratio (SNR) is reconsidered to estimate the

W. Wen is with the Department of Mechanical Engineering, The Hong Kong Polytechnic University, Hong Kong (e-mail: 17902061r@connect.polyu.hk).

G. Zhang and L.-T. Hsu are with the Interdisciplinary Division of Aeronautical and Aviation Engineering, The Hong Kong Polytechnic University, Hong Kong (e-mail: guo-hao.zhang@connect.polyu.hk; lt.hsu@polyu.edu.hk).

noise covariance of GNSS positioning. Deep coupling of GNSS and LiDAR is also researched [24], [25]. Another method to detect the NLOS receptions is the tight coupling of the GNSS receiver and omnidirectional camera [26], [27]. Skyline of buildings in the urbanized area can be detected to identify the NLOS satellites. However, this method cannot get satisfactory improvement in conditions with strong light, as the computer vision-based skyline detection is sensitive to light conditions.

Generally, these 3DMA GNSS can only mitigate multipath effects and NLOS receptions caused by buildings modeled in the 3D city maps. However, moving objects with a tall height, such as the double-decker bus [28] whose height can reach 4.5 meters, can also cause NLOS receptions. In particular, highly urbanized cities such as New York, London and Hong Kong possessing numerous double-decker buses in the streets, which can introduce considerable errors into the GNSS pseudorange measurements. This GNSS positioning error caused by moving objects cannot be mitigated by the novel 3DMA GNSS. To obtain better GNSS positioning performance for autonomous driving, this is a significant issue that needs to be considered.

In this paper, we propose to exclude the NLOS receptions caused by moving objects in heavy traffic urban scenarios using real-time 3D point cloud generated by LiDAR. The multiple-channel LiDAR is widely used in autonomous driving vehicles [29], [30] and is employed to provide distance information of surrounding environments. This paper innovatively takes advantage of LiDAR-based perception to assist the performance of GNSS positioning. In general, object detection is consisted of two parts, clustering (segmentation) [31]–[33] and classification [34], [35]. In this paper, the Euclidean clustering algorithm is employed to do clustering. The parameters-based method is presented for the double-decker bus classification. In this case, the dimension and position of the dynamic object relative to the GNSS receiver are calculated by object detection. Based on the boundaries of the detected object, NLOS exclusion can be implemented with our proposed exclusion algorithm. Moreover, the initial position of the GNSS receiver, which is significant for 3DMA GNSS, is also not required in our proposed NLOS exclusion algorithm. Finally, GNSS positioning result is calculated based on the surviving satellites. To the best of authors' knowledge, this paper is the first attempt to employ the object detection algorithm to depict the dynamic objects in GNSS Skyplot with the aid of 3D LiDAR equipped on the vehicle. In other words, this paper proposes an idea to employ LiDAR perception to aid GNSS absolute positioning.

The remainder of this paper is structured as follows. An overview of the proposed method is given in Section II. Section III discusses the double-decker bus detection method using the Euclidean clustering algorithm and parameter-based classification method. The coordinate transformation from LiDAR coordinate system to the GNSS Skyplot coordinate system is also presented in Section III. In Section IV, the NLOS exclusion criterion is proposed and satellite exclusion is implemented. Then, GNSS WLS positioning is introduced. In Section V, we evaluate the effectiveness of the
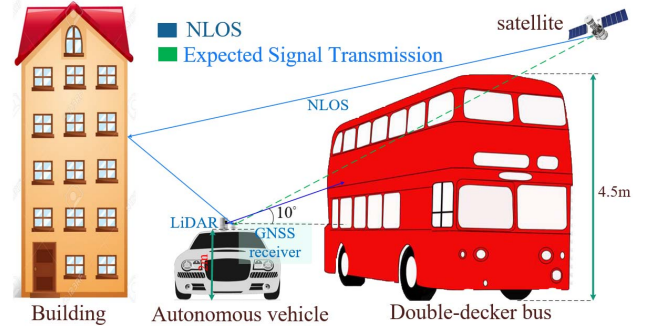

Fig. 1. Illustration of NLOS receptions caused by a double-decker bus. The double-decker bus causes the GNSS signal blockage. Surrounding objects such as the buildings are the possible reflectors subsequently.
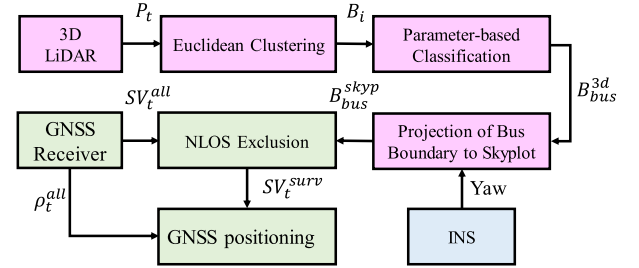

Fig. 2. Overview of the proposed algorithm of NLOS exclusion and GNSS positioning flowchart. Inputs are the 3D point cloud from 3D LiDAR, yaw angle from INS and raw measurements from GNSS receiver. The output is the GNSS positioning result based on the remaining satellites after NLOS exclusion.

proposed method by means of both static and dynamic experiments. Finally, conclusions are presented, and future work is discussed in Section VI.

II. OVERVIEW OF THE PROPOSED METHOD

In this study, we focus on the NLOS reception caused by the double-decker bus, a representative moving object in Hong Kong. Fig. 1 presents direct propagation routes and potential NLOS reception of the GNSS signal. The double-decker bus (height is 4.5 meters) can block signals transmitted from the satellite. Meanwhile, this GNSS signal can be reflected by nearby buildings and finally received by GNSS receiver equipped on top of the autonomous vehicle resulting in NLOS reception. This magnitude of pseudorange error of this NLOS is subjected to the distance from the GNSS receiver to the reflector and the elevation angle of the satellite [5].

As an essential sensor for positioning and perception of autonomous driving, 3D LiDAR is installed on the top as shown in Fig. 1. In this study, LiDAR is employed to detect the surrounding double-decker buses. Then, NLOS exclusion is implemented based on detected double-decker boundaries parameters which are projected into a Skyplot, which described the distribution of satellites in terms of elevation and azimuth angles [36]. Finally, GNSS WLS positioning is conducted using the remaining satellites. Fig. 2 shows the flowchart of the proposed algorithm: improved GNSS positioning by NLOS exclusion based on object detection of LiDAR point cloud. The inputs of the chart include two parts,

raw measurements and satellite information from GNSS and 3D point cloud by LiDAR. Moreover, the yaw angle from INS is also an input for coordinate transformation. The output is the GNSS positioning result. The proposed method can be executed as follows:

Step I: Euclidean clustering is employed to transfer real-time 3D point clouds into several clusters, so-called point cloud segmentation. The parameters-based classification method is utilized to classify the clusters and identify the double-decker bus from multi-clusters.

Step II: Satellites and the double-decker bus are projected into a Skyplot based on their azimuth and elevation angles relative to the GNSS receiver.

Step III: Considering satellite elevation, azimuth angles, SNR and double-decker bus boundary information (elevation and azimuth angles in Skyplot), satellites that blocked by double-decker bus are excluded.

Step IV: Implementing GNSS WLS positioning using the surviving satellites after the NLOS exclusion by Step III.

The details of the algorithms are introduced in the following sections.

III. DOUBLE-DECKER BUS DETECTION AND TRANSFORMATION

Due to the limited field of view (FOV), for example, $+10°$ to $-30°$ vertical FOV used this paper, the LiDAR can only scan part of the double-decker bus body as shown in Fig. 1. In this section, Euclidean clustering [37] and parameters-based classification methods [34] are employed to detect the double-decker bus. Moreover, the height of the detected double-decker bus is extended to the true height subsequently.

A. Clustering for Double-Decker Bus Detection

From the view of LiDAR, the surrounding environment is represented as numerous points at a given time t and the points are considered as a point set $P_t = \{p_1, p_2, \ldots, p_i, \ldots, p_n, t\}$, where $p_i = (x_i, y_i, z_i)$ represents a single point at a given time t in the LiDAR coordinate system. To give the points set P_t a physical meaning, Euclidean clustering is implemented to divide the point set into several organized sets. The process of the Euclidean clustering algorithm is summarized in Algorithm 1.

The output of Algorithm 1 is organized points sets $C_t^{clt} = \{C_1, C_2, \ldots, C_i, \ldots C_n, t\}$. To better portray the clusters, each cluster is represented by a descriptor, the bounding box [38]. Based on the principle of the bounding box, each C_i in C_t^{clt} can be transformed to B_i in $B_t^{clt} = \{B_1, B_2, \ldots, B_i, \ldots B_n, t\}$ and is specifically determined by vector B_i as follows:

$$B_i = \left[x_i^c, y_i^c, z_i^c, roll_i^c, pitch_i^c, yaw_i^c, d_i^{len}, d_i^{wid}, d_i^{al} \right] \quad (1)$$

where x_i^c, y_i^c and z_i^c denote the position of the bounding box in x, y, and z directions respectively in the LiDAR coordinate system. $roll_i^c$, $pitch_i^c$ and yaw_i^c denote the orientation of the bounding box. d_i^{len} is the length, d_i^{wid} is the width and d_i^{al} is the altitude of the bounding box. The bounding box list B_t^{clt} contains both double-decker buses and other objects.

Algorithm 1 Euclidean Clustering for Points Set P_t

Input: points set $P_t = \{p_1, p_2, \ldots, p_n, t\}$, search radius r_{search}

Output: organized points sets $C_t^{clt} = \{C_1, C_2, \ldots, C_i, \ldots C_n, t\}$

1 create a Kd-tree representation for the input points set P_t
2 set up an empty clusters list C_t^{clt} and an empty list to save organized point sets
3 **for all** points p_i in P_t **do**
4   add p_i to the points set P_t^{check}
5   **for all** p_i in P_t^{check} **do**
6   search for the points set N_i of point neighbor of p_i in a sphere with radius r $< r_{search}$
7   **for** every point N_i^i in points set N_i **do**
8   **if** N_i^i have not been processed
9   add N_i^i to points sets P_t^{check}
10   **end if**
11   **end for** the points set N_i
12   **if all** the points in P_t^{check} have been processed
13   add P_t^{check} to C_t^{clt}
14   reset P_t^{check} to empty
15   **end if**
16 **end for** P_t^{check}
17 **end for** P_t

B. Parameter-Based Double-Decker Bus Classification

To determine the double-decker bus clusters in the bounding box list B_t^{clt}, the parameter-based classification method is detailed in Algorithm 2. The output of Algorithm 2 is the bounding box set indicating the double-decker bus. If one cluster from C_t^{clt} is identified as a double-decker bus, the height for the corresponding bounding box will be extended to the real height d_{bus}^{al}.

Dimensions of the bounding box and geometry distribution corresponding to the cluster are all considered for classification. Cubic structure imposes the points in the cluster corresponding to the double-decker bus with specific geometry distribution. Thus, the standard deviation $\sigma_{p,i}^{cluster}$ of all the points is employed as a classification feature which is calculated as follows:

$$\sigma_{p,i}^{cluster} = \sqrt{\frac{\sum_{i=1}^{n} (p_i - \bar{p})^2}{n - 1}} \quad (2)$$

$$\bar{p} = \frac{\sum_{i=1}^{n} p_i}{n} \quad (3)$$

where n denotes the total number of points in one cluster. $\bar{p}$ represents the geometry center of the cluster. $(p_i - \bar{p})^2$ means the Euclidean distance between p_i and $\bar{p}$. The inputs of Algorithm 2 include bounding Box sets B_t^{clt}, organized point clusters C_t^{clt}, number of points threshold num_{thres}, etc. The function *Num* is used to calculate the number of points in a cluster. len_{min}, and len_{max} are used to identify the bounding box indicating the double-decker bus by the length of the bounding box. The functions of thresholds for length and height are the same as that of the length. As the ranging distance for LiDAR can go up to about 100 meters, thus

Algorithm 2 Double-Decker Bus Classification

Input: Bounding Box sets $B_t^{clt} = \{B_1, B_2, \ldots, B_i, \ldots B_n, t\}$, Organized point clusters $C_t^{clt} = \{C_1, C_2, \ldots, C_i, \ldots C_n, t\}$, point number threshold num_{thres}, true height d_{bus}^{al} of the double-decker bus, length threshold len_{min}, len_{max}, width threshold wid_{min}, wid_{max}, height threshold al_{min}, al_{max} and standard deviation threshold PV_{min}, PV_{max}.

Output: Bounding Box set represent double-decker bus $B_t^{clt\_bus} = \{B_1^{bus}, B_2^{bus}, \ldots, B_i^{bus}, \ldots B_n^{bus}, t\}$

1   set up an empty clusters list $B_t^{clt\_bus}$ to save bounding box
2   **for all** bounding box B_i in B_t^{clt} **do**
3   **if** $Num\ (C_i) > num_{thres}$
4     $B_i \leftarrow [x_i^c, y_i^c, z_i^c, roll_i^c, pitch_i^c, yaw_i^c, d_i^{len}, d_i^{wid}, d_i^{al}]$
5   **if** $d_i^{len} > len_{min}$ **and** $d_i^{len} < len_{max}$
6   **if** $d_i^{wid} > wid_{min}$ **and** $d_i^{wid} < wid_{max}$
7   **if** $d_i^{al} > al_{min}$ **and** $d_i^{al} < al_{max}$
8      $d_i^{al} \leftarrow d_{bus}^{al}$
9      $B_i^{bus} \leftarrow B_i$
10   **end if**
11   **end if**
12   **end if**
13   **end if**
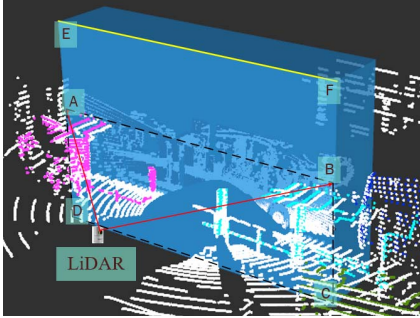14 **end for** B_t^{clt}

Fig. 3. Illustration of double-decker bus detection using the Euclidean cluster algorithm and parameters-based classification. Blue box ABCD represents the initially detected double-decker bus. Blue box ABFE represents the extended detected double-decker bus.

both width and length can be fully scanned when LiDAR is approaching the double-decker bus.

C. Representation of Double-Decker Bus

As illustrated previously, only part of the double-decker bus can be scanned by LiDAR which is represented by rectangle ABCD in Fig. 3. Meanwhile, as the bus surface is partially composed of the glass window, some parts of the bus are vacant from the view of LiDAR which can be seen in Fig. 3.

Dimension parameters of the bounding box representing the double-decker bus can be extended to the real one. The extended box is represented by rectangle AEFB in Fig. 3. Then, the boundary parameters for the double-decker bus as shown in Fig. 2 are denoted by the line segment $\overline{EF}$ denoted as B_{bus}^{3d}, the matrix of the bus boundary. To represent the bus, two points, E and F, are required. The B_{bus}^{3d} is structured as
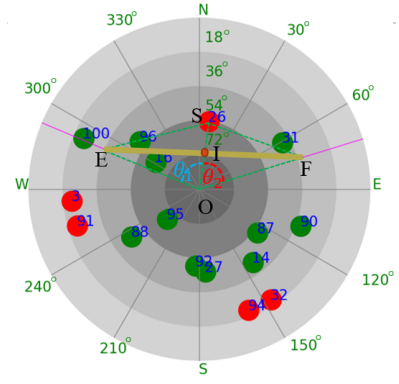

Fig. 4. Skyplot of GNSS satellites and detected double-decker bus boundary. Green circles and their associated numbers indicate satellites' PRNs. Line segment $\overline{EF}$ indicates the boundary.

follows:

$$B_{bus}^{3d} = \begin{bmatrix} x_{3dE} & y_{3dE} & z_{3dE} \\ x_{3dF} & y_{3dF} & z_{3dF} \end{bmatrix} \tag{4}$$

Thus, the double-decker bus boundary is detected.

D. Coordination Transformation

To implement the algorithm of NLOS exclusion, satellites' visibility needs to be determined based on the boundary of the double-decker bus. Thus, the relative position of the GNSS receiver to satellites and to the double-decker bus need to be transformed into the same representation, the Skyplot. In each epoch, satellite information, including azimuth, elevation angles, and SNR, can be acquired from the GNSS receiver. Satellites information can be represented as $SV_t^{all} = \{SV_1, SV_2, \ldots, SV_i, \ldots SV_n\}$. SV_i represents the information for satellite i and $SV_i = \{azim_i, ele_i, SNR_i\}$.

Satellite position can be easily indicated in the Skyplot representation that is 2-dimension coordinate based on corresponding elevation and azimuth angles. Proper transformation matrix should be employed for double-decker bus boundary transformation from 3 dimensions coordinate to 2 dimensions coordinate. The transformation is conducted as the following formula.

$$B_{bus}^{skyp} = B_{bus}^{3d} G_T \tag{5}$$

where B_{bus}^{3d} denotes the matrix of bus boundary presented in the previous sub-section. G_T is a 3×2 transform matrix indicating the yaw angle bias between the heading of LiDAR and north of earth, which can be obtained from the INS. The B_{dou}^{skyp} denotes the boundary matrix (2×2) in Skyplot structured as follows:

$$B_{bus}^{skyp} = \begin{bmatrix} x_{skyE} & y_{skyE} \\ x_{skyF} & y_{skyF} \end{bmatrix} \tag{6}$$

After the transformation, satellites and the double-decker bus can be presented in the same coordinate system, the Skyplot, as shown in Fig. 4. Line segment $\overline{EF}$ represents the double-decker bus boundary corresponding to the line segment $\overline{EF}$ as shown in Fig. 3. Then, the azimuth and the elevation angles for points E, and F can be calculated in the Skyplot respectively.

IV. IMPROVED GNSS POSITIONING BY NLOS EXCLUSION

In this section, the NLOS exclusion criterion is proposed based on the detected double-decker bus boundary, satellite elevation, azimuth angles, and SNR. Then, GNSS positioning is conducted by the WLS method.

A. NLOS Exclusion Based on Double-Decker Bus Boundary

To exclude the satellites blocked by the double-decker bus, the relative position between each satellite and the detected bus boundary needs to be calculated. As shown in Fig. 4, line segment $\overline{EF}$ represents the boundary of a double-decker bus. Satellite 26 (PRN 26) is located at point S. The azimuth and elevation angles are 8° and 54°, respectively. The satellite exclusion procedure is summarized in detail as shown in Algorithm 3. Inputs of Algorithm 3 are the satellite information SV_t^{all}, bus boundary matrix B_{bus}^{skyp}, the threshold of triangle area $S_{threshold}$, the threshold of SNR $SNR_{threshold}$ and threshold of boundary uncertainty θ_{thres}. Outputs of Algorithm 3 are the survived satellites after NLOS exclusion. **Firstly**, the angle θ_1 and θ_2 shown in Fig. 4 are estimated. Then areas of the triangle $S_{\Delta SEO}$, $S_{\Delta SFO}$, $S_{\Delta SEF}$ and $S_{\Delta EOF}$ are calculated and ΔS can be estimated subsequently. The ΔS is positive, it means that the satellite is outside the triangle ΔEOF and vice versa. The $(\theta_1 + \theta_2) < 180$ is employed to check if the satellite and the bus are on the same side with respect to the ego-vehicle. If the satellite is outside the triangle ΔEOF, it means that the satellite is possibly blocked by the double-decker bus and vice versa.

Secondly, GNSS measurement that SNR is larger than $SNR_{threshold}$ will not be excluded. To avoid the faulty exclusion, a heuristically determined threshold $S_{threshold}$ is set. Satellites whose positions are quite near the extended edge beam ($\theta_1 < \theta_{thres}$ or $\theta_2 < \theta_{thres}$) also should not be excluded, such as the satellite 100 in Fig. 4. Satellites whose positions are quite near the double-decker bus boundary should not be excluded which can be judged by ΔS, such as the satellites 31 and 96 in Fig. 4.

Finally, all the satellites in SV_t^{all} are indexed and the satellites that should not be excluded will be added to SV_t^{surv}. According to the proposed NLOS exclusion algorithm in Algorithm 3, satellites 3, 26, 91,94 and 32 are going to be excluded.

B. GNSS Positioning Based on Surviving Satellites

Measurements with low elevation angle and SNR are more likely to be a contaminated GNSS signal, such as the multipath or NLOS, due to the reflection, blockage, and diffraction. Thus, proper thresholds need to be set to exclude unhealthy measurements. For satellite SV_i, if ele_i of i_{th} satellite is less than a threshold ele_{thres}, it should be excluded from GNSS positioning.

The clock bias between the GNSS receiver and satellites is usually represented by the pseudorange measurements. The equation linking the receiver position and satellite can be structured as the following formula using least square (LS) method:

$$\hat{x} = (G^T G)^{-1} G^T \rho \qquad (7)$$

Algorithm 3 NLOS Exclusion Based on Bus Detection

Input: Satellites information set $SV_t^{all} = \{SV_1, SV_2, \ldots, SV_i, \ldots SV_n\}$, bus boundary matrix B_{bus}^{skyp}, area threshold $S_{threshold}$, SNR threshold $SNR_{threshold}$, the threshold of boundary uncertainty θ_{thres}

Output: surviving satellites set after NLOS exclusion: $SV_t^{surv} = \{SV_1, SV_2, \ldots, SV_i, \ldots SV_m\}$

1 **for all** satellites SV_i in SV_t^{all} **do**
2   estimate θ_1, θ_2 as shown in Fig. 4
3   Get triangle area $S_{\Delta SEO}$ of triangle SEO from B_{bus}^{skyp}
4   Get triangle area $S_{\Delta SFO}$ of triangle SFO from B_{bus}^{skyp}
5   Get triangle area $S_{\Delta SEF}$ of triangle SEF from B_{bus}^{skyp}
6   Get triangle area $S_{\Delta EOF}$ of triangle EOF from B_{bus}^{skyp}
7   $\Delta S = S_{\Delta SEO} + S_{\Delta SFO} + S_{\Delta SEF} - S_{\Delta EOF}$
8   **if** $(SNR_i > SNR_{threshold})$ or $(\theta_1 < \theta_{thres})$ or $(\theta_2 < \theta_{thres})$
9   add SV_i to satellites set SV_t^{surv} and **break**
10   **if** $\Delta S > S_{threshold}$ **and** $((\theta_1 + \theta_2) < 180°)$
11   **break**
12   **else**
13   add SV_i to satellites set SV_t^{surv}
14   **end if**
15 **end for** satellites set SV_t^{all}

---

where G represents the observation matrix and is structured by unit LOS vectors between GNSS receivers' position and satellite position. $\hat{x}$ indicates the estimated receiver position and ρ denotes the pseudorange measurements.

To better represent the reliability of each measurement based on the information measured by the receiver, the weightings of each satellite are needed. Function to calculate the weighting by integrating the measurement SNR and satellite elevation is expressed as [39]:

$$
\begin{aligned}
&W^{(i)}(ele_i, SNR_i) \\
&= \begin{cases}
\dfrac{1}{sin^2 ele_i} \\
\quad \times \left(10^{-\frac{(SNR_i - T)}{a}}\left(\left(\dfrac{A}{10^{-\frac{(F-T)}{a}}} - 1\right)\dfrac{(SNR_i - T)}{F - T} + 1\right)\right) \\
\quad SNR_i < SNR_{threshold} \\
1 \quad SNR_i \geq SNR_{threshold}
\end{cases}
\end{aligned}
$$

$$(8)$$

where $W^{(i)}(ele_i, SNR_i)$ denotes the weighting for satellite SV_i. Parameter a, A and F in (8) are experimentally determined. Then, the weighting matrix W is a diagonal matrix constituted by the weighting $W^{(k)}(ele_i, SNR_i)$. Finally, the GNSS receiver position can be estimated using the WLS method as:

$$\hat{x} = (G^T W G)^{-1} G^T W \rho \qquad (9)$$

Note that both LS (7) and WLS (8) positioning methods are compared in the experiment section.

TABLE I
PARAMETER VALUES USED IN THIS PAPER

Parameters	$S_{threshold}$	$SNR_{threshold}$	ele_{thres}	θ_{thres}
Value	10	45 dB-Hz	20°	5°
Parameters	a	A	F	
Value	30	32	10	

V. EXPERIMENT EVALUATION

A. Experiment Setup

A static experiment is firstly conducted near a bus stop in Hong Kong with a double-decker bus around to evaluate the magnitude of NLOS errors caused by the double-decker bus. By selecting an obvious landmark in the vicinity of the testing environment, we got the actual position of tested static position by referencing the landmark position labeled in Google Maps. In our experience, the accuracy is within about 1 meter. The dynamic experiment is implemented in urban scenarios of Hong Kong to demonstrate the effectiveness of the proposed method. We use the RTK GNSS/INS integrated system (NovAtel SPAN-CPT, RTK/INS integrated navigation system with fiber optics gyroscopes) to provide high accuracy ground truth. This device is commonly used for ground truth of positioning among academic fields and industry fields. The u-blox M8T receiver is used to collect raw GPS and BeiDou measurements. 3D LiDAR sensor, Velodyne 32, is employed to provide the real-time point cloud.

For the static experiment, both u-blox receiver and 3D LiDAR are installed on a fix position near a static double-decker bus during the experiment. The data were collected at a frequency of 1 Hz. For the dynamic experiment, both u-blox receiver and 3D LiDAR are installed on the top of a vehicle running on an urbanized road.

To verify the effectiveness of the proposed method, four methods were compared, the "EF" represents the "elevation filter". This means that the elevation angle threshold is applied.

(1). LS positioning (LS)
(2). LS positioning $+ele_{thres}$ (LS-EF)
(3). WLS positioning $+ele_{thres}$ (WLS-EF)
(4). WLS positioning $+ele_{thres}$ + NLOS exclusion (WLS-EF-NE)

In this experiment section, the setting of the parameters mentioned above can be found in TABLE I.

B. Comparison of Different GNSS Positioning Methods Using Static Data

The static experimental scenario is shown in Fig. 5. As the double-decker bus is near the LiDAR sensor, boundary matrix B_{bus}^{skyp} is always available throughout the static test. The experiment results of GNSS positioning using four methods are shown in TABLE II.

The LS method can achieve only 70.59 meters of mean absolute error (MAE) and 81.53 meters of root mean square error (RMSE) among the test. Approximately 88.29 % of the MAE results have a positioning error of more than 40 meters. With the aid of elevation angle filters, the MAE and RMSE of LS-EF are decreased to 51.91 and 62.34 meters, respectively.
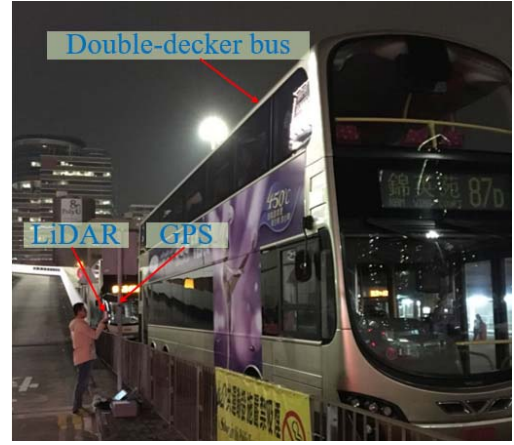

Fig. 5. An environment that the data were collected at a bus stop. Satellites can be blocked by the double-decker bus.

TABLE II
POSITIONING PERFORMANCE OF THE FOUR METHODS
NEAR A BUS STOP (IN THE UNIT OF THE METER)

All data	LS	LS-EF	WLS-EF	WLS-EF-NE
MAE	70.59m	51.91m	47.16m	22.76m
Std	26.0m	29.4m	32.34m	18.59m
RMSE	81.53m	62.34m	57.09m	27.96m
Percentage (MAE<15 meters)	5.81%	11.35%	14.58%	38.00%
Percentage (MAE<30 meters)	9.12%	28.11%	34.46%	77.61%
Percentage (MAE>40 meters)	88.29%	63.24%	50.14%	8.83%
Mean number of excluded satellites		3.13	3.13	5.98

About 63.24 % of the results of MAE possess a large error (> 40 meters). Meanwhile, the percentage of MAE results less than 20 meters is improved from 5.81 % to 11.3 %. This indicates that the elevation filter can enhance the positioning by excluding the unhealthy measurements. The reason behind this improvement is the exclusion of measurements from satellite 3, 91 and 22, which can be seen in Fig. 6. Those satellites possess low elevation, about 19°, are suffering from severe NLOS and/or multipath effects, thus introducing considerable positioning errors. The mean number of NLOS satellites is 3.13 throughout the test. A slight improvement is obtained using WLS-EF comparing with that of the LS-EF method. The MAE is decreased to 47.16 meters. This enhanced result indicates that weighting shown in (8) can effectively represent the health level for each measurement.

With the proposed NLOS exclusion method, the positioning results are considerably improved. Firstly, the positioning error and standard deviation (Std) of WLS-EF-NE are reduced to 22.76 and 18.59 meters, respectively, comparing to that of the WLS-EF method. Secondly, almost 38 % of the results have a small positioning error (<15 meters). Moreover, only 8.83 %
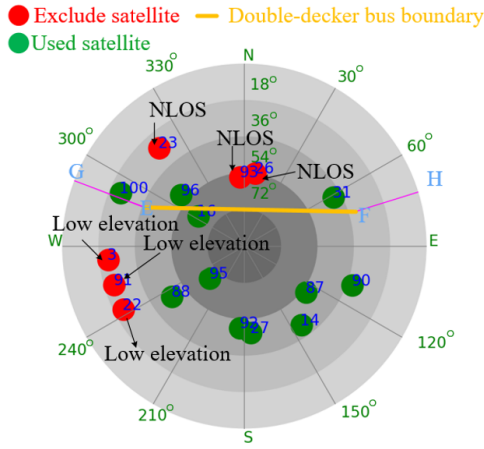
Fig. 6. Skyplot indicating the satellite distribution during the static experiment. The green circle represents the satellites that are healthy, which will be used in GNSS positioning. The red circle denotes the excluded satellites. The yellow line indicates the double-decker bus boundary.
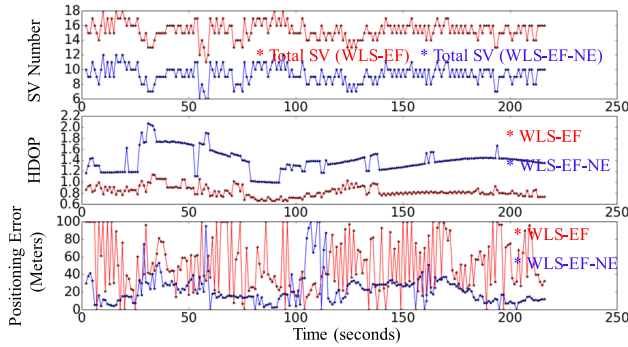

Fig. 7. Experimental results of WLS-EF and WLS-EF-NE, which depicted in red and blue dots, respectively. The top panel indicates the number of satellites used. Middle panels indicate the HDOP values. Botton panel indicates the 3D positioning errors.

of the results possess an error of more than 40 meters. The reason for this improvement is the proposed NLOS exclusion as shown in Fig. 6. Satellites 23, 26 and 93 are excluded using the proposed algorithm 3. Though the three satellites are blocked by double-decker bus, GNSS signals from them are reflected by surrounding buildings in the double-decker bus station, thus causing the erroneous NLOS receptions. HDOP, positioning error and the numbers of measurement used in the WLS-EF-NE and WLS-EF method are shown in Fig. 7. The total satellites are over 10 all through the test, thus the availability of GNSS positioning solution is 100 %. After the NLOS exclusion, the HDOP value shown in the second panel is slightly increased, due to the change in the geometry distribution of satellites.

C. Evaluation of WLS-EF Positioning With Manual Exclusion Using Static Data

This sub-section presents the results of WLS-EF with a manual exclusion, meaning a specific measurement is excluded before using the WLS-EF method. TABLE III shows the results of four separated exclusion tests. Exclusion of satellite 23 introduces a slight improvement in positioning

TABLE III

POSITIONING PERFORMANCE OF WLS-EF WITH SINGLE SATELLITE EXCLUSION (IN THE UNIT OF THE METER)

All data	PRN23	PRN26	PRN93	PRN100
MAE	42.5m	32.31m	46.51m	55.08m
Std	27.53m	26.67m	30.01m	30.28m
RMSE	47.65m	39.50m	56.94m	67.75m
Percentage (MAE<15 meters)	15.33%	18.51%	6.38%	4.12%
Percentage (MAE<30 meters)	37.71%	67.72%	38.29%	25.13%
Percentage (MAE>40 meters)	45.90%	23.28%	45.74%	59.16%
Improvement (Mean error)	4.66m (9.8%)	14.8m (31.38%)	0.65m (1.42%)	-7.92m (worsen: -16.79%)

performance with an MAE of 42.5 meters, comparing to the MAE of 47.16 meters using the WLS-EF method without exclusion. As the GNSS signal received from satellite 23 is NLOS. Similarly, exclusion of satellites 26 and 93 also obtain improvements with an MAE of 32.31 meters and 46.51 meters respectively. The reason for this improvement's distinction is that satellite 26 suffered larger NLOS errors comparing to satellites 93 which is subjected to the environment's features. According to [5], the NLOS delay in the pseudorange domain is related to the ground distance from the receiver to the surrounding objects that reflect the signal, and the satellite elevation angle. The satellite with larger ground distance and lower elevation angle is more likely to cause larger NLOS error. Signals from satellites 26 and 93 can be reflected by different objects, respectively. However, the ground distances, denoted by α_1 and α_2, between the receiver and the two separate reflectors can be distinct (α_1 for satellite 26, α_2 for satellite 93). α_1 can be considerably larger than α_2, therefore causing greater positioning error. On the contrary, greater improvement will be introduced if satellite 26 is excluded from GNSS positioning comparing with satellite 93.

After the exclusion of satellite 26, 67.72 % of the results possess an MAE less than 30 meters. However, the exclusion of satellite 100 introduces larger MAE comparing to the no exclusion situation. The MAE increases to 55.08 meters and approximately 59.16 % of the results possess an MAE of more than 40 meters. The reason for this worsen performance is that satellite 100 is not blocked by double-decker bus though it is quite near the extended edge beam (line segment $\overline{EG}$ in Fig. 6). Thus, excluding satellites 23, 26 and 93 can all obtain improvements in GNSS positioning due to the double-decker bus blockage and subsequent NLOS receptions.

D. Comparison of Different GNSS Positioning Methods Using Dynamic Data

The dynamic experimental scenario is shown in Fig. 8 and Fig. 11, with a GNSS receiver and LiDAR sensor installed on a vehicle driven in urban areas.
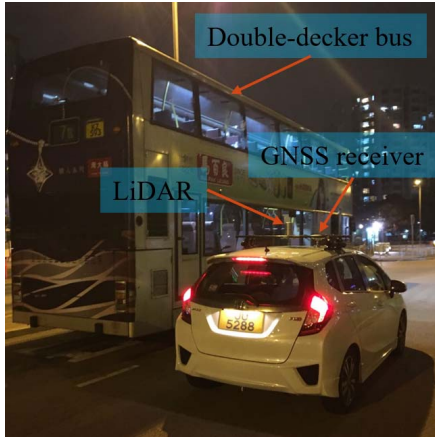
Fig. 8. The environment that the data were collected in an urban scenario in Hong Kong. Satellites can frequently be blocked by the double-decker.
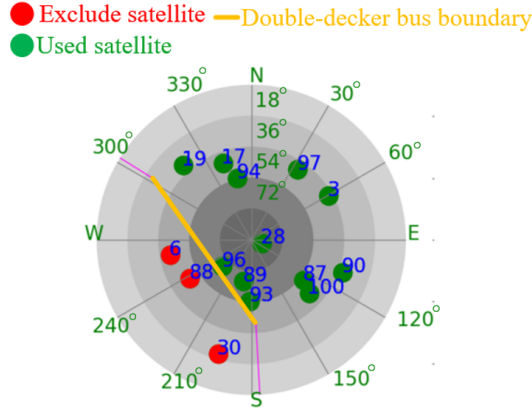

Fig. 9. Skyplot snapshot indicating the satellite distribution during the dynamic experiment. The green circle represents the satellites that are healthy, which will be used in GNSS positioning. The red circle denotes the excluded satellites. The yellow line indicates the double-decker bus boundary.
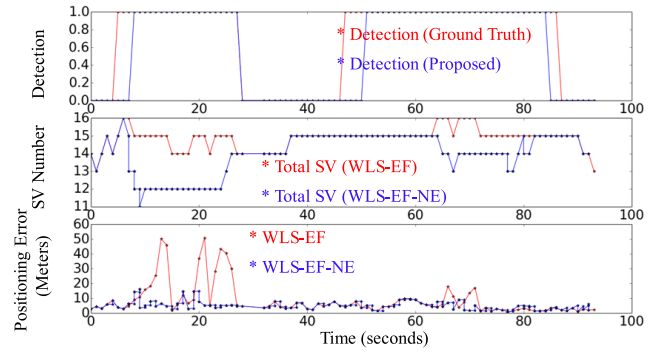

Fig. 10. Experimental results of WLS-EF and WLS-EF-NE in the dynamic experiment, which depicted in red and blue dots, respectively. The top panel indicates the double-decker bus detection result. The middle panel indicates the numbers of satellites used. The bottom panel indicates the 3D positioning errors.
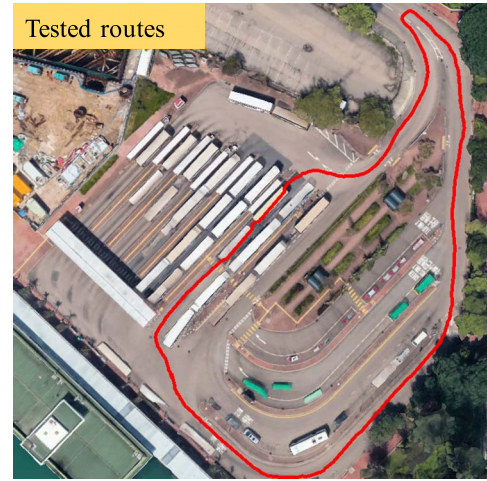

Fig. 11. Illustration of tested routes in the dynamic experiment (plotted in Google Earth). The red curve indicates the ground truth of tested routes provided by NovAtel SPAN-CPT.

As the testing vehicle is driven on the road, the boundary matrix B_{bus}^{skyp} is frequently available throughout the dynamic test. Similar to Fig. 6, the Skyplot representing one epoch in the test can be seen in Fig. 9. Satellite 6, 30 and 88, with elevations of 41°, 23°, and 46° respectively, are excluded, due to the blockage from the double-decker bus.

There are still about 12 satellites including GPS and BeiDou remained which are enough for further GNSS positioning. The experiment results of GNSS positioning using WLS-EF and WLS-EF-NE are shown in Fig. 10 and the only discrepancy of the two methods is NLOS exclusion proposed in this paper.

The top panel denotes the double-decker bus detection performance through the test. Detection accuracy of 90.43 % is obtained with the proposed double-decker bus detection method. The failure in double-decker-bus detection usually occurs when the LiDAR is approaching or leaving the double-decker bus. This is because of the limited FOV of LiDAR and only a few parts of the bus can be scanned which only provides few points. The middle panel indicates the satellite numbers using WLS-EF and WLS-EF-NE throughout the test. Approximately 2 to 4 satellites are excluded during the test

when there is a double-decker bus. We can see from Fig. 10 that there two times that the double-decker bus causes NLOS. The bottom panel indicates the GNSS positioning accuracy through the dynamic test. The positioning errors can be effectively reduced with the NLOS exclusion of those blocked satellites. The positioning errors are all reduced to less than 20 meters with the proposed method, compared with the conventional method (WLS-EF) whose positioning errors can go up to even 50 meters in Fig. 10. TABLE IV shows the GNSS positioning performance using four positioning methods.

The LS method can achieve only 47.59 meters of MAE and 58.61 meters of RMSE among the dynamic test. Approximately 29.71 % of the result possess an error smaller than 5 meters and 60.35 % of the results have a positioning error of more than 15 meters. With the aid of elevation filters, the MAE and RMSE of LS-EF are decreased to 44.98 and 52.17 meters, respectively. About 55.81 % of the results are larger than 15 meters, which indicates the improvements introduced by the elevation angle filters. Considerable improvements are provided by the WLS-EF method with the $W^{(i)}$ (ele_i, SNR_i).

TABLE IV

POSITIONING PERFORMANCE OF THE FOUR METHODS IN THE DYNAMIC TEST (IN THE UNIT OF THE METER)

All data	LS	LS-EF	WLS-EF	WLS-EF-NE
MAE	47.59m	44.98m	13.19m	5.04m
Std	42.07m	40.99m	14.67m	2.87m
RMSE	58.61m	52.17m	16.58m	6.29m
Percentage (MAE<5 meters)	29.71%	30.23%	46.51%	53.49%
Percentage (MAE<10 meters)	37.16%	41.86%	60.47%	95.35%
Percentage (MAE>15 meters)	60.35%	55.81%	30.23%	0%

The MAE is decreased to 13.19 meters and about 46.51 % of the results have an MAE of less than 5 meters. Moreover, only 30.23 % of the results possess large errors (> 15 meters) and the standard deviation drops dramatically comparing with the LS-EF method.

With the proposed method, decent improvements are obtained. Firstly, the positioning error declines from 13.19 meters to 5.04 meters in the tested dynamic experiment, which obtains about 61.79 % of the improvements, compared with the WLS-EF method. The standard deviation drops from 14.67 to 2.87 meters. Interestingly, 53.49 % of the results have an MAE of less than 5 meters and approximately 95.35 % of the results possess errors less than 10 meters. Both GNSS positioning accuracy and standard deviation are improved by using the proposed method.

VI. CONCLUSION AND FUTURE WORK

With the rise of GNSS, more satellites are available including GPS, BeiDou, GLONASS and Galileo. The number of visible satellites is still enough for GNSS positioning even after NLOS exclusion. This study firstly employs an object detection algorithm to detect a double-decker bus and extend its dimensions to a real one. Then, the proper coordinate transformation is utilized to project the double-decker bus boundary into GNSS Skyplot. NLOS exclusion criterion integrating elevation angle, SNR and bus boundary is proposed. According to the experiment result, the proposed method obtains the best performance among the four conventional GNSS positioning methods. Positioning error of NLOS receptions caused by a double-decker bus can reach 24 meters in the static experiment and 8 meters improvement in the evaluated dynamic experiment. The magnitude of the improvement is subjected to the environment features. Finally, we conclude that the exclusion of NLOS receptions is necessary for obtaining better GNSS positioning accuracy in urbanized cities.

Regarding future work, only one LiDAR is employed to scan the surrounding vehicles. Due to the object detection demand and decreased prices of 3D LiDAR sensors, a multi-LiDAR based sensor setup is common in autonomous vehicles. The 3D LiDARs are installed with a different slant angle, in this case, the vertical field of view angle range can be increased to more than 75 degrees. Therefore, the other tall dynamic vehicles can also be detected. We are planning to

equip our vehicle with multi-LiDAR to detect the surrounding dynamic vehicles. Moreover, the new dynamic experiment will be conducted in the urbanized area with complicated traffic conditions by integrating the proposed method and the 3DMA GNSS technique. In this case, both the static building and moving objects are considered to facilitate GNSS positioning. The performance of the integrated method under dynamic scenarios will be studied.

REFERENCES

[1] J. Levinson and S. Thrun, "Robust vehicle localization in urban environments using probabilistic maps," in *Proc. IEEE Int. Conf. Robot. Automat. (ICRA)*, May 2010, pp. 4372–4378.

[2] Y. Gu, L.-T. Hsu, and S. Kamijo, "GNSS/onboard inertial sensor integration with the aid of 3-D building map for lane-level vehicle self-localization in urban canyon," *IEEE Trans. Veh. Technol.*, vol. 65, no. 6, pp. 4274–4287, Jun. 2016.

[3] A. Fernández *et al.*, "GNSS/INS/LiDAR integration in urban environment: Algorithm description and results from ATENEA test campaign," in *Proc. 6th ESA Workshop Satell. Navigat. Technol. (Navitec) Eur. Workshop GNSS Signals Signal Process.*, Dec. 2012, pp. 1–8.

[4] L.-T. Hsu, H. Tokura, N. Kubo, Y. Gu, and S. Kamijo, "Multiple faulty GNSS measurement exclusion based on consistency check in urban canyons," *IEEE Sensors J.*, vol. 17, no. 6, pp. 1909–1917, Mar. 2017.

[5] L.-T. Hsu, "Analysis and modeling GPS NLOS effect in highly urbanized area," *GPS Solutions*, vol. 22, no. 1, p. 7, 2018.

[6] S.-H. Kong, "Statistical analysis of urban GPS multipaths and pseudo-range measurement errors," *IEEE Trans. Aerosp. Electron. Syst.*, vol. 47, no. 2, pp. 1101–1113, Apr. 2011.

[7] J. Breßler, P. Reisdorf, M. Obst, and G. Wanielik, "GNSS positioning in non-line-of-sight context—A survey," in *Proc. IEEE 19th Int. Conf. Intell. Transp. Syst. (ITSC)*, Nov. 2016, pp. 1147–1154.

[8] Y. Suh and R. Shibasaki, "Evaluation of satellite-based navigation services in complex urban environments using a three-dimensional GIS," *IEICE Trans. Commun.*, vol. 90, no. 7, pp. 1816–1825, 2007.

[9] C. Pinana-Diaz, R. Toledo-Moreo, D. Bétaille, and A. F. Gómez-Skarmeta, "GPS multipath detection and exclusion with elevation-enhanced maps," in *Proc. 14th Int. IEEE Conf. Intell. Transp. Syst. (ITSC)*, Oct. 2011, pp. 19–24.

[10] M. Obst, S. Bauer, P. Reisdorf, and G. Wanielik, "Multipath detection with 3D digital maps for robust multi-constellation GNSS/INS vehicle localization in urban areas," in *Proc. IEEE Intell. Vehicles Symp.*, Jun. 2012, pp. 184–190.

[11] S. Peyraud *et al.*, "About non-line-of-sight satellite detection and exclusion in a 3D map-aided localization algorithm," *Sensors*, vol. 13, no. 1, pp. 829–847, 2013.

[12] Y.-W. Lee, Y.-C. Suh, and R. Shibasaki, "A simulation system for GNSS multipath mitigation using spatial statistical methods," *Comput. Geosci.*, vol. 34, no. 11, pp. 1597–1609, 2008.

[13] L.-T. Hsu, F. Chen, and S. Kamijo, "Evaluation of multi-GNSSs and GPS with 3D map methods for pedestrian positioning in an urban canyon environment," *IEICE Trans. Fundam. Electron., Commun. Comput. Sci.*, vol. 98, no. 1, pp. 284–293, 2015.

[14] P. D. Groves, "Shadow matching: A new GNSS positioning technique for urban canyons," *J. Navigat.*, vol. 64, no. 3, pp. 417–430, 2011.

[15] L. Wang, P. D. Groves, and M. K. Ziebart, "Multi-constellation GNSS performance evaluation for urban canyons using large virtual reality city models," *J. Navigat.*, vol. 65, no. 3, pp. 459–476, 2012.

[16] L. Wang, P. D. Groves, and M. K. Ziebart, "GNSS shadow matching: Improving urban positioning accuracy using a 3D city model with optimized visibility scoring scheme," *Navigation*, vol. 60, no. 3, pp. 195–207, 2013.

[17] L. Wang, P. D. Groves, and M. K. Ziebart, "Smartphone shadow matching for better cross-street GNSS positioning in urban environments," *J. Navigat.*, vol. 68, no. 3, pp. 411–433, 2015.

[18] S. Miura, L.-T. Hsu, F. Chen, and S. Kamijo, "GPS error correction with pseudorange evaluation using three-dimensional maps," *IEEE Trans. Intell. Transp. Syst.*, vol. 16, no. 6, pp. 3104–3115, Dec. 2015.

[19] L.-T. Hsu, Y. Gu, and S. Kamijo, "3D building model-based pedestrian positioning method using GPS/GLONASS/QZSS and its reliability calculation," *GPS Solutions*, vol. 20, no. 3, pp. 413–428, 2016.

[20] L.-T. Hsu, Y. Gu, Y. Huang, and S. Kamijo, "Urban pedestrian navigation using smartphone-based dead reckoning and 3-D map-aided GNSS," *IEEE Sensors J.*, vol. 16, no. 5, pp. 1281–1293, Mar. 2016.

[21] M. Adjrad and P. D. Groves, "Intelligent urban positioning: Integration of shadow matching with 3D-mapping-aided GNSS ranging," *J. Navigat.*, vol. 71, no. 1, pp. 1–20, 2018.

[22] M. Adjrad and P. D. Groves, "Enhancing least squares GNSS positioning with 3D mapping without accurate prior knowledge," *Navigation*, vol. 64, no. 1, pp. 75–91, 2017.

[23] D. Betaille, F. Peyret, M. Ortiz, S. Miquel, and F. Godan, "Improving accuracy and integrity with a probabilistic urban Trench modeling," *Navigation*, vol. 63, no. 3, pp. 283–294, 2016.

[24] D. Maier and A. Kleiner, "Improved GPS sensor model for mobile robots in urban terrain," in *Proc. IEEE Int. Conf. Robot. Automat. (ICRA)*, May 2010, pp. 4385–4390.

[25] K. Ali, X. Chen, F. Dovis, D. De Castro, and A. J. Fernández, "GNSS signal multipath error characterization in urban environments using LiDAR data aiding," in *Proc. IEEE 1st AESS Eur. Conf. Satell. Telecommun. (ESTEL)*, Oct. 2012, pp. 1–5.

[26] J.-I. Meguro, T. Murata, J.-I. Takiguchi, Y. Amano, and T. Hashizume, "GPS multipath mitigation for urban area using omnidirectional infrared camera," *IEEE Trans. Intell. Transp. Syst.*, vol. 10, no. 1, pp. 22–30, Mar. 2009.

[27] T. Suzuki, M. Kitamura, Y. Amano, and T. Hashizume, "High-accuracy GPS and GLONASS positioning by multipath mitigation using omni-directional infrared camera," in *Proc. IEEE Int. Conf. Robot. Automat.*, May 2011, pp. 311–316.

[28] O. O. Okunribido, S. J. Shimbles, M. Magnusson, and M. Pope, "City bus driving and low back pain: A study of the exposures to posture demands, manual materials handling and whole-body vibration," *Appl. Ergonom.*, vol. 38, no. 1, pp. 29–38, Jan. 2007.

[29] J. Levinson *et al.*, "Towards fully autonomous driving: Systems and algorithms," in *Proc. IEEE Intell. Vehicles Symp. (IV)*, Jun. 2011, pp. 163–168.

[30] J. Wei, J. M. Snider, J. Kim, J. M. Dolan, R. Rajkumar, and B. Litkouhi, "Towards a viable autonomous driving research platform," in *Proc. IEEE Intell. Vehicles Symp. (IV)*, Jun. 2013, pp. 763–770.

[31] M. Himmelsbach, F. V. Hundelshausen, and H.-J. Wuensche, "Fast segmentation of 3D point clouds for ground vehicles," in *Proc. IEEE Intell. Vehicles Symp.*, Jun. 2010, pp. 560–565.

[32] W. Li, Q. Guo, M. K. Jakubowski, and M. Kelly, "A new method for segmenting individual trees from the lidar point cloud," *Photogramm. Eng. Remote Sens.*, vol. 78, no. 1, pp. 75–84, 2012.

[33] B. Douillard *et al.*, "On the segmentation of 3D LIDAR point clouds," in *Proc. IEEE Int. Conf. Robot. Automat. (ICRA)*, May 2011, pp. 2798–2805.

[34] P. Gehler and S. Nowozin, "On feature combination for multiclass object classification," in *Proc. IEEE 12th Int. Conf. Comput. Vis.*, Sep./Oct. 2009, pp. 221–228.

[35] J. Zhang, X. Lin, and X. Ning, "SVM-based classification of segmented airborne LiDAR point clouds in urban areas," *Remote Sens.*, vol. 5, no. 8, pp. 3749–3775, 2013.

[36] J. Marshall, "Creating and viewing skyplots," *GPS solutions*, vol. 6, nos. 1–2, pp. 118–120, 2002.

[37] R. B. Rusu, "Semantic 3D object maps for everyday manipulation in human living environments," *KI-Künstliche Intell.*, vol. 24, no. 4, pp. 345–348, 2010.

[38] G. Barequet and S. Har-Peled, "Efficiently approximating the minimum-volume bounding, box of a point set in three dimensions," *J. Algorithms*, vol. 38, no. 1, pp. 91–109, Jan. 2001.

[39] A. M. Herrera, H. F. Suhandri, E. Realini, M. Reguzzoni, and M. C. J. G. S. de Lacy, "goGPS: Open-source MATLAB software," *GPS Solutions*, vol. 20, no. 3, pp. 595–603, 2016.
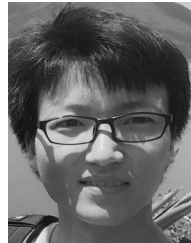
Weisong Wen was born in Ganzhou, Jiangxi, China. He is currently pursuing the Ph.D. degree in mechanical engineering with The Hong Kong Polytechnic University. His research interest includes the GNSS/INS/LiDAR/HD map-based localization for autonomous vehicles. He is also a Visiting Student Researcher with the University of California, Berkeley (UCB).

Guohao Zhang received the bachelor's degree in mechanical engineering and automation from the University of Science and Technology Beijing, China, in 2015, and the master's degree in mechanical engineering from The Hong Kong Polytechnic University. He is currently a Research Assistant with The Hong Kong Polytechnic University. His research interests include GNSS urban localization, vehicle-to-vehicle cooperative localization, and multisensor integrated navigation.

Li-Ta Hsu received the B.S. and Ph.D. degrees in aeronautics and astronautics from National Cheng Kung University, Taiwan, in 2007 and 2013, respectively. He served as a Post-Doctoral Researcher with the Institute of Industrial Science, University of Tokyo, Japan. In 2012, he was a Visiting Scholar with University College London, U.K. He is currently an Assistant Professor with the Division of Aeronautical and Aviation Engineering, The Hong Kong Polytechnic University. His research interests include GNSS positioning in challenging environments and localization for pedestrian, autonomous driving vehicle, and unmanned aerial vehicle. He is an Associate Fellow of RIN.